Deliverable D4.5

Report on role of granularity in magnon nano-reservoirs

Project Number	101070290
Project name	Nonlinear Magnons for Reservoir Computing in Reciprocal Space
Project acronym	NIMFEIA
Work Package	WP4 Materials and device fabrication
Type	Report
Dissemination Level	Public
Lead Beneficiary	INL
Due date of delivery	Month 30 – March 2025

Disclaimer:

The NIMFEIA project has received funding by the European Union's Research and Innovation Programme Horizon Europe under grant agreement No 101070290. However, views and opinions expressed in this document are those of the authors only and do not necessarily reflect those of the European Union. The European Union cannot be held responsible for them.

1 Introduction

This document acts as an overview of the impact of granular defects with respect to the operation of magnetic tunnel junctions in the context of reservoir computing.

The goal of the deliverable is to provide a description of impact of granular defects in a variety of magnetic materials and thicknesses in order to assess their impact on the device quality. Additional some preliminary attempts to harness the impact of the granularity is presented in the context of a novel physical unclonable function for cryptography appplications.

2 Device fabrication and materials

The devices under investigation are magnetic tunnel junctions (MTJ), consisting of a complex set of magnetic layers. An example of such a magnetic stack is 6 IrMn / 2 $CoFe_{30}$ / 0.7 Ru / 2.6 $CoFe_{40}B_{20}$ / MgO [8 ohm um2] / 2.0 $CoFe_{40}B_{20}$ / 0.21 Ta / 7 NiFe, where the CoFeB/Ta/NiFe composite is considered to be the free layer, whose magnetisation can vary. The free layer will have a magnetic vortex as the ground state for diameters d > 200 nm, where the in-plane magnetisation will form increasingly small circular loops, whose sense of rotation will define the vortex core chirality, and a central out of plane vortex core, whose direction will define the polarity of the vortex. The CoFeB is required for correct crystallisation of the MgO layer, and the NiFe layer is chosen as a soft magnetic material. The Ta dusting layer stops interaction in crystal texture between the NiFe and CoFeB layer. The CoFe/Ru/CoFeB is a synthetic antiferromagnet (SAF) with the upper layer acting as the fixed layer, whose magnetisation remains fixed.

NiFe is a polycrystalline material and is the basis of much extensive previous work on vortex-based oscillators [1–8]. Recently, the impact of the grains on the device performance has been investigated [9], and an alternative solution in the form of CoFeSiB has been suggested. CofeSiB is amorphous even after standard MTJ annealing processes (330C, 1T, 2 hours) which are required for high quality devices.

Internal reference	Stack details (thickness in nanometres)	Description
VPW42	6 IrMn / 2 $CoFe_{30}$ / 0.825 Ru / 2.6 $CoFe_{40}B_{20}$ / MgO [8.2 Ohm um2] / 1.25 $CoFe_{40}B_{20}$ / 0.21 Ta / 5 CoFeSiB	CoFeSiB 5nm free layer^{+}
VPW32	6 IrMn / 2 CoFe30 / 0.825 Ru / 2.6 CoFe40B20 / MgO [8 Ohm um2] / 2.0 CoFe40B20 / 0.21 Ta / 18 CoFeSiB	CoFeSiB 18nm free layer^{+}
VPW46	6 IrMn / 2 $CoFe_{30}$ / 0.825 Ru / 2.6 $CoFe_{40}B_{20}$ / MgO [8 Ohm um2] / 2.0 $CoFe_{40}B_{20}$ / 0.21 Ta / 40 CoFeSiB	CoFeSiB 40nm free layer^{+}
VPW32	6 IrMn / 2 $CoFe_{30}$ / 0.825 Ru / 2.6 $CoFe_{40}B_{20}$ / MgO [8 Ohm um2] / 2.0 $CoFe_{40}B_{20}$ / 0.21 Ta / 80 CoFeSiB	CoFeSiB 80nm free layer^{+}
VPW50	6 IrMn / 2 $CoFe_{30}$ / 0.825 Ru / 2.6 $CoFe_{40}B_{20}$ / MgO [6 Ohm um2] / 2.0 $CoFe_{40}B_{20}$ / 0.21 Ta / 160 CoFeSiB	CoFeSiB 160nm free layer^{+}
VPW43	6 IrMn / 2 $CoFe_{30}$ / 0.7 Ru / 2.6 $CoFe_{40}B_{20}$ / MgO [8 ohm um2] / 2.0 $CoFe_{40}B_{20}$ / 0.21 Ta / 7 NiFe	Standard NiFe free layer*

$^{+}$ - conventional process,
* - new process

Table 1 – overview of devices fabricated in the context of the NIMFEIA project

This project has received funding from the EU Research and Innovation Programme Horizon Europe under grant agreement No 101070290.

3 Characterising the impact of the granular defects on vortex-based magnetic tunnel junction reservoir operation

3.1.1 Micromagnetic modelling

In order to understand the impact of the granular defects on the dynamics associated with vortex-based magnetic tunnel junctions, micromagnetic simulations were performed. The micromagnetic simulations were performed using the mumax3 code for 500 nm nanopillars with typical NiFe material parameters (M_{sat} = 740x10^3 A/m, A_{ex} = 1.3x10^{-11} J/m, alpha = 0.01). Although the pinning defects could be caused by other means (i.e. roughness [10]), in these simulations the local pinning defects were introduced by creating a random granular structure [11]. The nanopillar was separated into individual grains with an average size of 20 nm (values of the grain size in NiFe in the literature vary between 4 and 10 nm in ref. [11], 35 and 85 nm in ref. [12], 30 nm in ref [13]). The lower end of the range of grains sizes was selected as the free layer in this study is relatively thin (t_{NiFe} = 7nm) and the grain size tends to increase with thickness [10]. Local pinning sites were created by randomly varying the saturation magnetisation of the grains between M_{sat} and 0.85*M_{sat} and the inter-region exchange at the boundaries between the grains was also reduced to 0.85*A_{ex} at the granular interface.

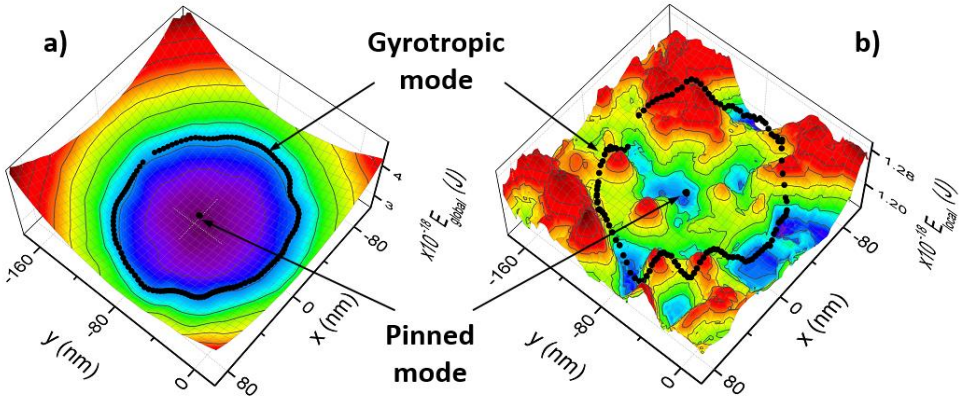

Figure 1 – Energy landscape simulations - Energy landscape calculated with micromagnetic simulations considering a) the whole nanopillar and b) a 16 nm radius around the vortex core. The black dots shows typical trajectories of the sub-threshold pinned mode and the super-threshold gyrotropic mode.

In Figure 1, the energy landscape has been plotted as a function of the x and y position within the nanopillar. The simulations were performed by initialising a magnetic vortex at different lateral positions (i.e., x and y) and waiting for a short time period (i.e. ~0.1 ns) for the core to stabilise and calculating the subsequent energy, which comprises of the demagnetising, exchange and Zeeman component energy terms. In Figure 1 a), the energy of the whole of the nanopillar is calculated, and results in a standard parabolic potential minima. Although the granular defects are very slightly visible, the majority of the energy landscape is dominated by the edges of the nanopillar, with the in-plane part of the magnetic vortex typically being > 500 times in size compared to the vortex core.

This project has received funding from the EU Research and Innovation Programme Horizon Europe under grant agreement No 101070290.

In Figure 1 b), however, the energy landscape is again calculated, except this time only the energy within an area comparable to the vortex core (i.e. a circle with radius r = 16 nm) is calculated, and the local energy minima felt by the vortex core is presented. The impact of the granular defects is now much more pronounced, with lots of local maxima and minima visible. To illustrate the sub-threshold and super-threshold dynamics, typical trajectories of the vortex core when strongly pinned and after escaping the pinning site (i.e. the gyrotropic mode) are plotted.

In order to expand further on the different types of vortex core pinning, the energy of the vortex core is presented in Figure 2 a) with the corresponding vortex core trajectory when resonantly excited. In addition, the constituent energy terms of the total core energy, i.e. the exchange and demagnetisation energy of the vortex core are presented in Figure 2 b) and c), respectively, as a function the vortex core position. The energy landscape in terms of the exchange and demagnetisation are quite dissimilar, with the exchange energy consisting of a large number of small local minima and maxima, whereas the demagnetisation energy is a broader central minima. In Figure 2 d) and e), the variation of the exchange coupling and saturation magnetisation are plotted, where the exchange between grains is reduced by 15 % as discussed in the main text, and the magnetisation is randomly varied between 15% across the grain regions.

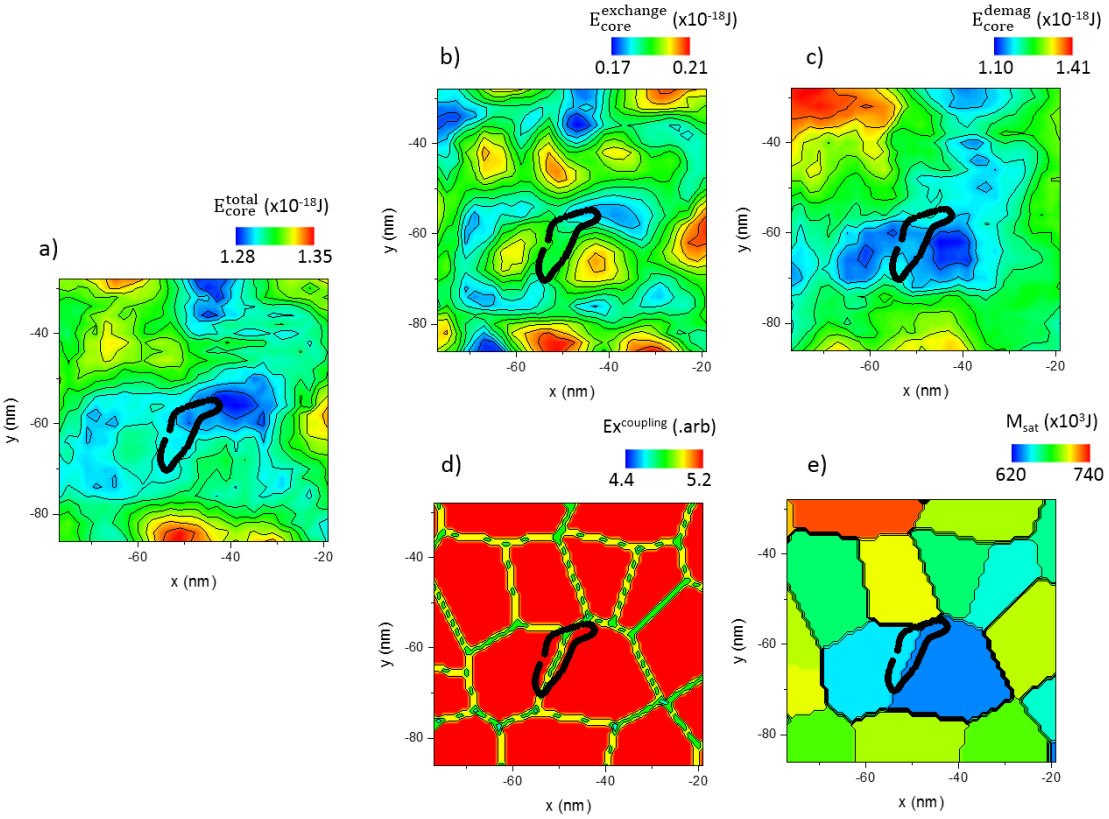

Figure 2 – The a) total b) exchange and c) demagnetisation energy of the vortex core and the variation in the d) exchange coupling at the grain boundary and e) variation of the saturation magnetisation as a function of the core position, x and y, for a magnetic field of Hx = -4.2 and Hy = 3.3 mT.

This project has received funding from the EU Research and Innovation Programme Horizon Europe under grant agreement No 101070290.

In Figure 3, the vortex core is located in a different part of the magnetic nanopillar with a different energy minima (and resonant frequency). The exchange energy and demagnetisation energy are again plotted (Figure 3 b and c), and again look very different with the exchage energy having characteristic small energy minima and the demagnetisation energy having a single broader minima and maxima.

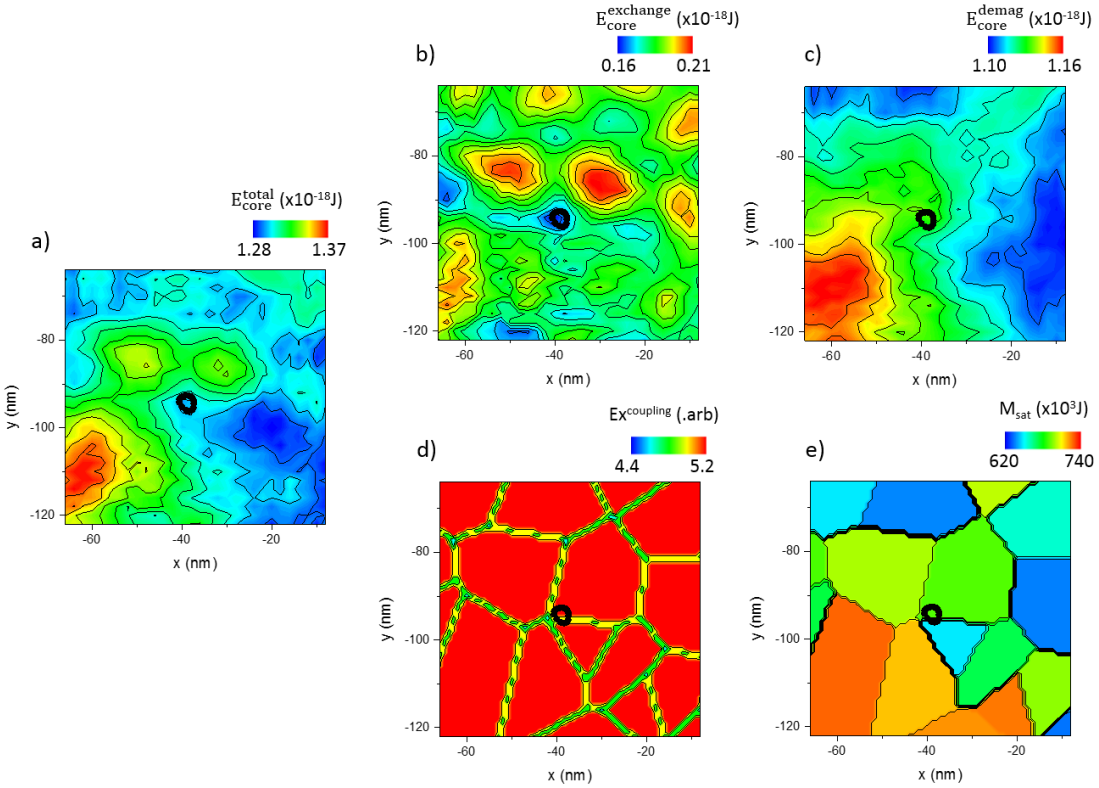

Figure 3 – The a) total b) exchange and c) demagnetisation energy of the vortex core and the variation in the d) exchange coupling at the grain boundary and e) variation of the saturation magnetisation as a function of the core position, x and y, for a magnetic field of Hx = -5.4 and Hy = 2.6 mT.

Comparison of the two pinning sites presented in Figure 2 and Figure 3 leads to certain conclusions with regard to the nature of the vortex core pinning. In Figure 2 the vortex core pinning is dominated by the relatively spatially large energy minima which is created by the presence to two grains with relatively reduced saturation magnetisation which results in a broad resonant response close to the gyrotropic frequency. The resonant response is close to the gyrotropic response, but with the core trajectory also being strongly modified by the nearby local grain boundary and subsequent variation in the exchange coupling. By contrast, in Figure 3 the relatively spatially small minima that the vortex core becomes trapped in is located where four grain boundaries intercept. This spatially small energy minima results in a high resonant frequency as discussed in the main text.

The impact of the grains can therefore be thought of existing between two extremes: firstly where the energy minima is dominated by a variation of the saturation magnetisation in grains resulting in a broad energy minima with a low resonant frequency and secondly a relatively small energy minima dominated by the grain boundaries and a high resonant frequency.

This project has received funding from the EU Research and Innovation Programme Horizon Europe under grant agreement No 101070290.

3.1.2 Experimental characterisation of granular defects

3.1.2.1 Static resistance measurements

The impact of the local energy minima which have been shown via the micromagnetic simulation can be seen be measuring the resistance of the device as a function of the in-plane magnetic field, Figure 4. For large negative in-plane magnetic fields the free layer is saturated opposite to the fixed reference layer and the resistance is large due to the tunnelling magnetoresistance effect, and inversely for large positive magnetic fields the free layer is parallel to the fixed layer and the device resistance is low. For field close to zero there is an intermediate resistance level which corresponds to the free layer being in the vortex state, but with a relatively large or small resistance depending on the position of the vortex core, i.e. how much of the vortex magnetisation is aligned either anti-parallel or parallel to the fixed layer. Instead of a smooth in-plane magnetic field dependence, for both VPW10 and VPW43 there are abrupt jumps in resistance, during which the resistance changes. For VPW10 these transition are pronounced and demonstrate clear hysteresis, corresponding to the vortex core being strongly trapped in a local minima. For VPW43 the resistive transition appear but do not demonstrate any hysteresis, discussed in more detail later in the report. The pronounced difference between these two devices show how even with identical free layers but with different capping layers, the granular defects can result in very different behaviours.

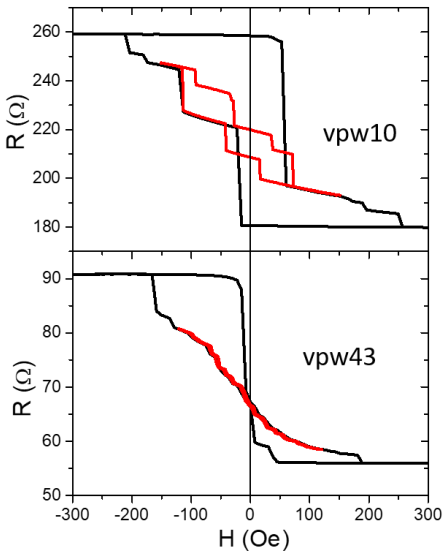

Figure 4 – resistance versus in-plane magnetic field for two NiFe free layers with different capping layers (i.e. vpw10 has CuN capping layer and vpw43 has Ta capping layer). Red curve shows a minor loop.

3.1.2.2 Dynamic measurements

In Figure 5 a), the absolute value of the rectified spin-diode voltage is presented as a function of the excitation frequency and power for a vMTJ, where the absolute value of the rectified voltage was

This project has received funding from the EU Research and Innovation Programme Horizon Europe under grant agreement No 101070290.

chosen so as to allow a log colour scale, in order for both the pinned and gyrotropic modes to be visible on the same graph. In reality, the spin diode response has an approximate anti-Lorentz lineshape [14], which crosses zero around the central resonant frequency. The black line which increases as a function of power (labelled the pinned mode) is therefore the central frequency of the pinned mode, and is constant over several orders of magnitude of excitation power, but starts to shift to lower frequencies as the power is increased.

The spin-diode presented in Figure 5 a) shows the presence of a clear threshold, P_{rf}^{t} (illustrated in the figure with a white line), below which the vortex core is pinned, and above which the core escapes the pinning sites and enters the gyrotropic mode. This type of threshold behaviour is consistent with results which have been previously explored optically on NiFe nano-disks [15]. The in-plane magnetic field dependence of the dynamic response is plotted in Figure 5 b) and c), for excitation frequencies above and below P_{rf}^{t}, (i.e. P_{rf} = 10 and 150 µW, respectively).

The frequency of the sub-threshold mode can be seen to vary strongly as a function of the in-plane magnetic field, whereas the super-threshold behaviour has a more constant frequency response, at frequencies consistent with the gyrotropic motion of the vortex core published in the literature (e.g. refs. [16,17]) and predicted by the modified Thiele equation [18].

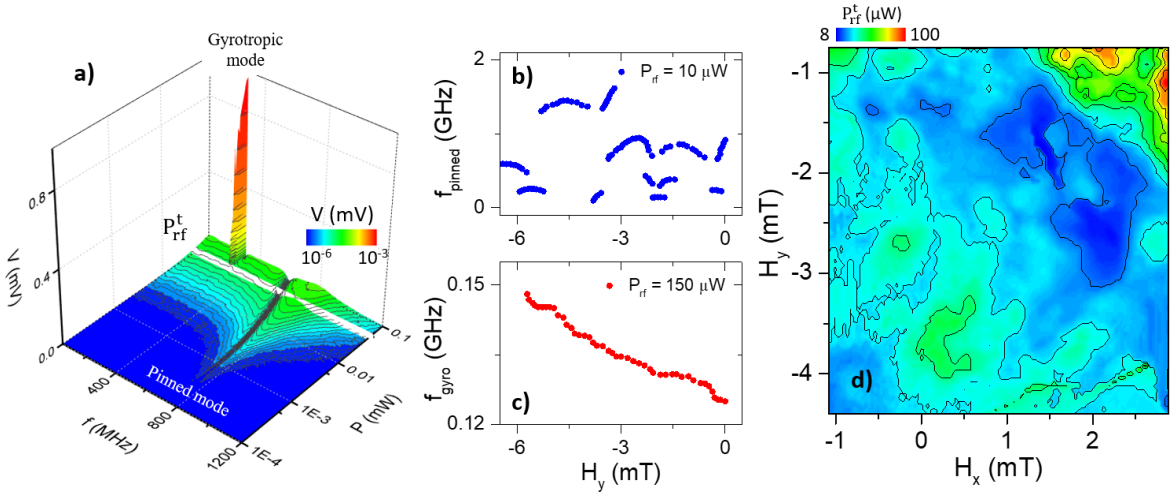

Figure 5 – Influence of pinning on spin-diode measurements a) Absolute magnitude of the experimentally determined spin-diode voltage as a function of the excitation frequency and power with the white line showing the threshold power, P_{rf}^{t}, at which the vortex core escape the pinning site and the resonant frequency of b) the pinned mode (Prf = 10 µW) and c) the gyrotropic mode (Prf = 150 µW). d) The threshold radio-frequency power, P_{rf}^{t}, as a function of the magnetic field applied along the x- and y-axis for an excitation current of fgyro = 115 MHz.

In fact, the value of the threshold power, P_{rf}^{t}, can be relatively easily determined experimentally and is plotted in Figure 5 d) as a function of the in-plane field. A radio-frequency of f = 115 MHz is applied to the MTJ, corresponding to the gyrotropic mode of the vortex confined in a d = 500 nm nanopillar, and the power at which the measured rectified voltage exceeds a critical value (i.e. V_{th} = 0.2 mV) is

This project has received funding from the EU Research and Innovation Programme Horizon Europe under grant agreement No 101070290.

determined. The threshold power can be seen to vary significantly (from 8 to 100 µW), with the value depending strongly on the value of the in-plane magnetic field, and therefore the location of the vortex core.

In order to validate the micromagnetic simulations with the experimental data in the sub-threshold regime, in Figure 6, the frequency of the pinned mode is determined as a function of the in-plane magnetic field (both transverse and along the MTJ easy axis, i.e. Hx and Hy respectively). The frequency was determined via FFT analysis of the magnetisation aligned along the easy-axis in the micromagnetic simulations, i.e. the m_y component, as the magnetic vortex relaxes over 50 ns. As the magnetic vortex relaxes towards equilibrium, a clear peak in frequency can be detected in the FFT of the m_y component, which is considered to be the relaxation frequency of the vortex in the pinned state. In Figure 6, this data is compared to the experimentally determined resonant frequency for a low, i.e. sub-threshold, excitation power of P_{rf} = 10 µW. The experimental resonance frequency is determined by sweeping the low power rf current, and extracting the central frequency of the dc voltage response, corresponding to the resonant frequency.

There is good agreement between the experimentally acquired spin-diode effect and the micromagnetic simulations, with the resonant frequency varying strongly as a function of the in-plane magnetic field, with different regions of similar resonant frequency corresponding to different pinning sites.

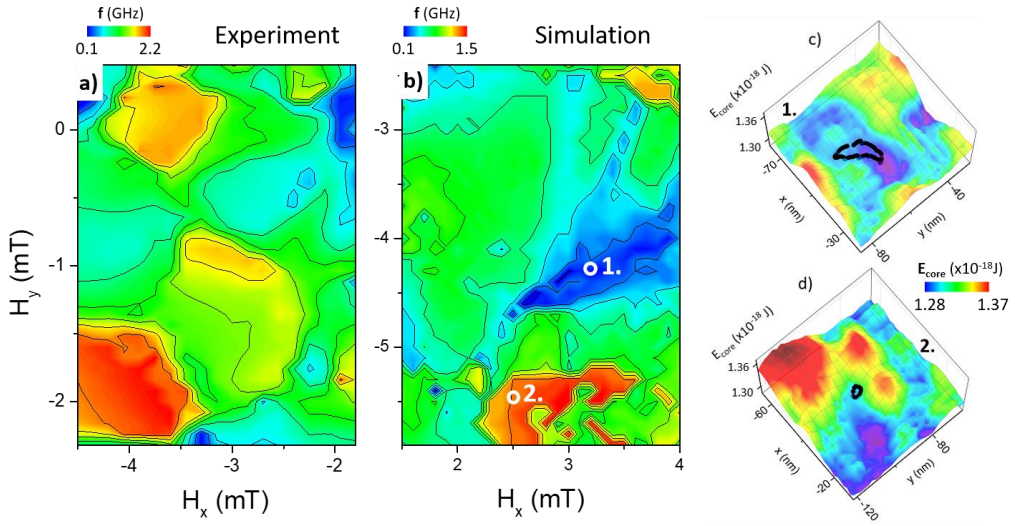

Figure 6 – Frequency variation at different pinning sites - Resonant frequency of the sub-threshold pinned mode as determined a) experimentally via spin diode effect and via b) micromagnetic simulations, as a function of the in-plane magnetic field (Hx and Hy). Energy landscape as calculated with micromagnetic simulations for two different in-plane magnetic fields i.e. c) Hx = -4.2mT and Hy = 3.3 and d) Hx = -5.4 mT and Hy = 2.6 mT. The black line corresponds to the trajectory of the vortex core when excited with an rf signal of 1 mA and a frequency of 220 MHz.

To further explore the different pinning sites and their consequent effect on the vortex dynamics, two magnetic fields were identified in Figure 6 b) (i.e [Hx, Hy] = -4.2, 3.3 mT and [Hx ,Hy] = -5.4,2.6

This project has received funding from the EU Research and Innovation Programme Horizon Europe under grant agreement No 101070290.

mT, labelled 1 and 2 respectively) with very different resonant frequencies (f_1 = 220 MHz and f_2 = 1400 MHz). These two fields correspond to a weakly pinned system (i.e. position 1) and a strongly pinned system (i.e. position 2). The energy landscapes calculated via micromagnetic simulations of these two different field values are presented in Figure 6 c) and d). Additionally, the typical trajectories of the sub-threshold pinned mode are presented for two resonant excitations (f_1 = 220MHz and f_2 = 1400 MHz for an excitation current of 1 mA). For position 1, the loosely pinned vortex core has a resonant frequency close to the global gyrotropic frequency, and the core is excited to relatively large orbits. This pinning site is spatially larger and is caused by two grains of relatively low saturation magnetisation being located next to one another. In the case of position 2, the strongly pinned core can be resonantly excited by applying a frequency far from the global gyrotropic mode, and results in a relatively small orbit. This energy minima is caused by the intersection of multiple grain boundaries which result in a pronounced yet spatially localised minima. The origin of the pinning site appears to have a pronounced impact on the vortex core dynamics leading to the possibility that analysis of the resonant frequency of the vortex core and subsequent comparison to micromagnetic simulations may provide an interesting tool for exploration of the granular structure of magnetic materials in the future.

The pinning of the vortex core will have a strong impact on the ability of the device to operate as a nano-reservoir, as the issues related to the device to device performance will have to be considered. As well as impacting the fundamental gyrotropic mode, the grains will also impact the higher order spin wave modes which are central to the reciprocal space reservoir paradigm. The impact on the spin wave modes can be seen in Figure 7, where the rectified spin diode voltage is plotted as a function of the in-plane magnetic field for an excitation, Prf = 1µW, for which the vortex is still pinned by the local defects. The spin wave modes can be seen to be separated into different field regimes, i.e. the frequency of the modes are relatively constant within a certain field range but these are separated into discrete distinct regimes.

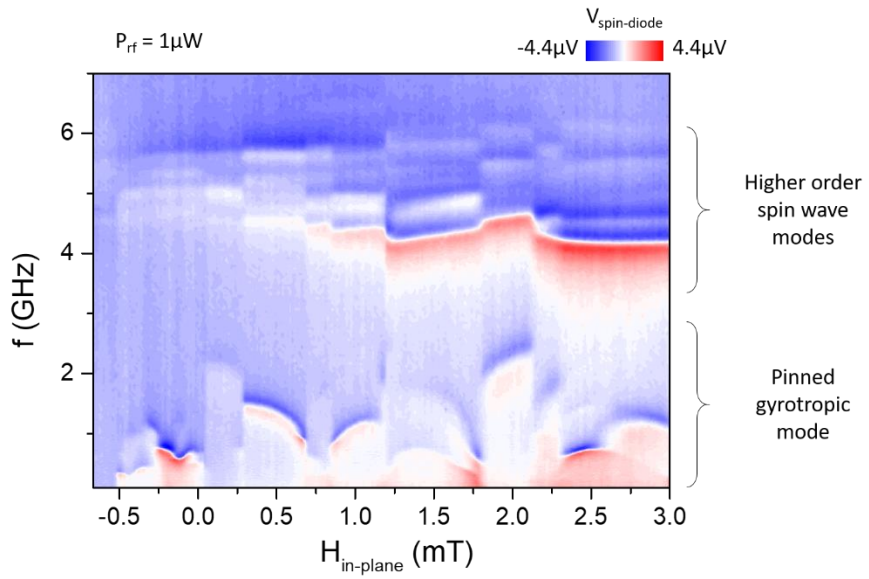

Figure 7 – spin diode voltage as a function of the applied current frequency, f_{source}, and in-plane magnetic field for an excitation power P_{rf} = 1 µW.

This project has received funding from the EU Research and Innovation Programme Horizon Europe under grant agreement No 101070290.

3.1.3 Exploring the pinning in the time domain

The in-plane magnetic field dependence of a typical MTJ is presented in Figure 8 a), for a field applied along the y-axis (i.e. collinear with the pinning layer). For a strong positive in-plane magnetic field the device resistance saturates at a maximum level, indicating the free layer is in a uniform state, anti-parallel to the pinned layer. For a strong negative field, the resistance saturates at a minimum indicating the free layer is in the uniform state parallel to the pinned layer. Around zero field, there is a relatively linear variation in resistance as a function of the in-plane field, which is indicative of the magnetic vortex, where the red line shows a minor loop of magnetic field.

At zero applied magnetic field, the magnetic vortex core will be located at the centre of the nanopillar, and if an in-plane magnetic field is applied, the magnetisation component aligned with the magnetic field will increase, resulting in a displacement of the vortex core. The exact position of the vortex core, therefore, depends on the exact applied in-plane magnetic field.

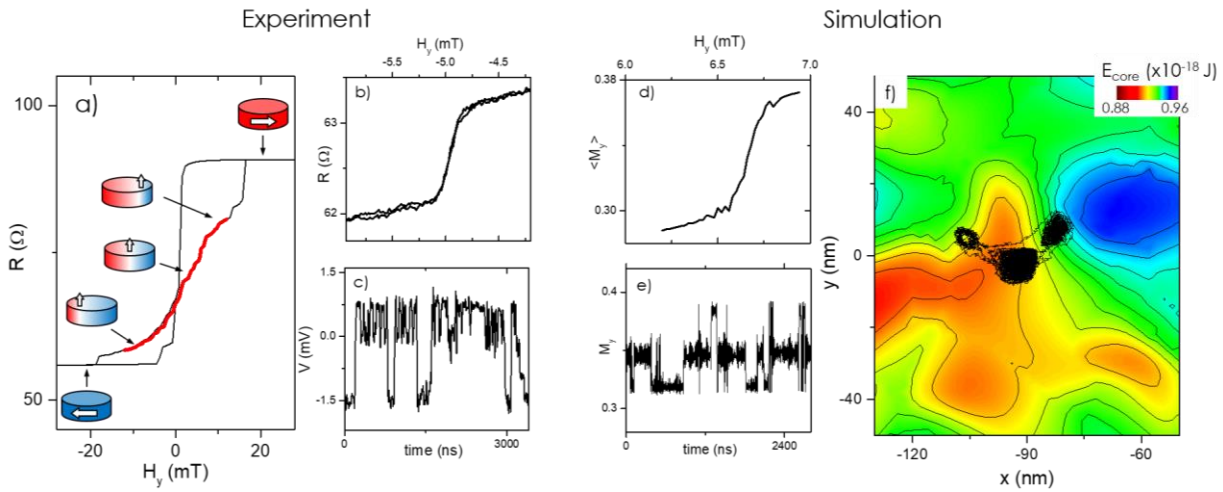

Figure 8 – resistance versus in-plane magnetic field for a) full and b) zoom sweep and c) the voltage as a function time for three different in-plane magnetic fields measured experimentally. Micromagnetic simulations were performed which qualitatively agreed, showing the d) magnetisation along the y-axis as a function of in-plane field and e) as a function of time as well as the energy landscape produced by the granular defects and the resultant vortex core trajectory between different local energy minima.

The resistance of the MTJ depends upon the relative orientation of the magnetisation between the free layer and the pinned reference layer, and as the vortex core is displaced, the resistance varies. Whilst there is a quasi-linear dependence on the resistance as a function of field, there are in fact more fine details in the field dependence, with regions of relatively small change in resistance separated by regions with a strong variation in resistance as a function if the in-plane field, as shown in Figure 8 b).

In order to understand these resistive jumps, the temporal evolution of the voltage has been measured. The device is connected to a bias tee, and a dc current of I = 10 mA is applied to the device, and the AC voltage is measured and is presented in Figure 8 c). In this case, the AC voltage shows the component of the resistance which is varying rapidly with time. The AC voltage at H_y = -

This project has received funding from the EU Research and Innovation Programme Horizon Europe under grant agreement No 101070290.

5mT can clearly be seen to jump between different discrete values as a function of time, characteristic of a superparamagnetic transition [19–21]. The jump in dc resistance observed in Figure 8 b) is a time averaging of these superparamagnetic transitions and shows there is a finite probability of being at a certain voltage level, which is dependent on the in-plane magnetic field. Unlike typical super-paramagnetic MTJ devices [22], which typically transition stochastically between two binary states, due to the complex energy landscape, the nanometer vortex core can be found in multiple pinning energy minima.

Micromagnetic simulations were performed at 100 K in order to better understand these resistive jumps. In the simulations the magnetisation along the y-axis is presented as this is analogous to the resistance, as the tunnel magnetoresistance is TMR = R_{AP}-R_P/R_P, and as the pinned layer is aligned along the y-axis, i.e. M_y = -1 and M_y = +1, correspond to the high anti-parallel and low parallel resistance states. A magnetic field was selected where the variation in the magnetisation along the y-axis was shown to have a sharp variation a function of magnetic field, i.e. Figure 8 d), which is analogous to the resistance value measured experimentally, i.e. Figure 8 b). In this region, i.e. Hy = -6.6 mT, the magnetisation transitions between multiple different discrete levels. This data is similar to the experimental data shown in Figure 8 c) which shows the ac voltage transitioning between multiple discrete levels.

In order to better understand this effect, the vortex core energy landscape was calculated by initialising a magnetic vortex at different lateral positions (i.e. x and y coordinates) and waiting for a short time period (i.e. ~0.1 ns) for the core to stabilise and calculating the subsequent energy within an area comparable to the vortex core (i.e. a circle with radius r = 16 nm). The energy landscape as a function of the vortex core position in x and y is shown in Figure 8 f) has maxima (red) and minima (blue) due to the granularities in the system. The trajectory of the vortex core for an applied field of H_y = 6.6 mT, i.e. the data shown in Figure 8 e), is plotted on to the energy landscape. The landscape which is induced by the granular defects is extremely complex, with a large maxima separating two minima, with a smaller saddle point located at the global minima.

3.1.4 Synchronisation of stochastic core transitions

In Figure 9, an oscillating magnetic field is produced by passing an AC current of frequency 1 MHz into a vertically integrated field line ~500nm above the MTJ free layer, which produces an in-plane magnetic field around 0.1 mT per mA applied to the field line. In Figure 9 a) the AC voltage is measured for a locking signal in the field line with a power P_{AC} = 6 dBm. Even though the locking signal is sinusoidal, the resultant AC voltage appears to switch between two discrete states. To better understand this, micromagnetic simulations were performed with a locking signal of a AC magnetic in-plane field B_{ac} = 0.1 mT. The simulations show a non-sinusoidal deterministic response, where the magnetisation also switches between two discrete levels. When this driven trajectory is plotted on the energy landscape, shown in Figure 9 b), where the vortex core is constantly driven between two different pronounced energy minima.

In Figure 9 c) the AC locking field is increased for both the experiment, i.e. P_{AC} = 17 dBm, and simulation, B_{ac} = 0.3 mT. In this case, as can be seen in the energy landscape in Figure 9 d), the system is again driven deterministically, however, this time between multiple discrete levels,

This project has received funding from the EU Research and Innovation Programme Horizon Europe under grant agreement No 101070290.

corresponding to many different energy minima as the increased driving field causes a larger displacement of the vortex core.

In Figure 9 e) the magnitude at 1 MHz of a fast fourier transform (FFT) of the experimentally measured AC voltage is presented as a function of the in-plane magnetic field and the rf power. When the AC voltage is locked there is a response at 1 MHz (the driving frequency) and when the AC voltage is not locked there is a relatively small response. Three different regimes as a function of the driving power are observed. At very low powers (i.e. P_{FL} ~ -20 dBm) there is little response for all values of in-plane magnetic field, i.e. the driving 1 MHz signal is insufficient to cause locking and the system oscillates super-paramagnetically. As the rf power is increased (i.e. P_{FL} = -10dBm) the response at 1 MHz increases, but only at certain in-plane magnetic fields (i.e. -5.1, -4.2, -3.6, -2.4 mT), indicating that the AC voltage locked to the driving signal, but that this only occurs at specific fields where the vortex is loosely pinned between energy minima, discussed in Figure 8. As the power continues to increase (i.e. P_{FL} > 0 dBm), the FFT starts to overlap and there is a finite response for all values of in-plane field, corresponding to the vortex core being driven across multiple different pinning sites (or energy minima).

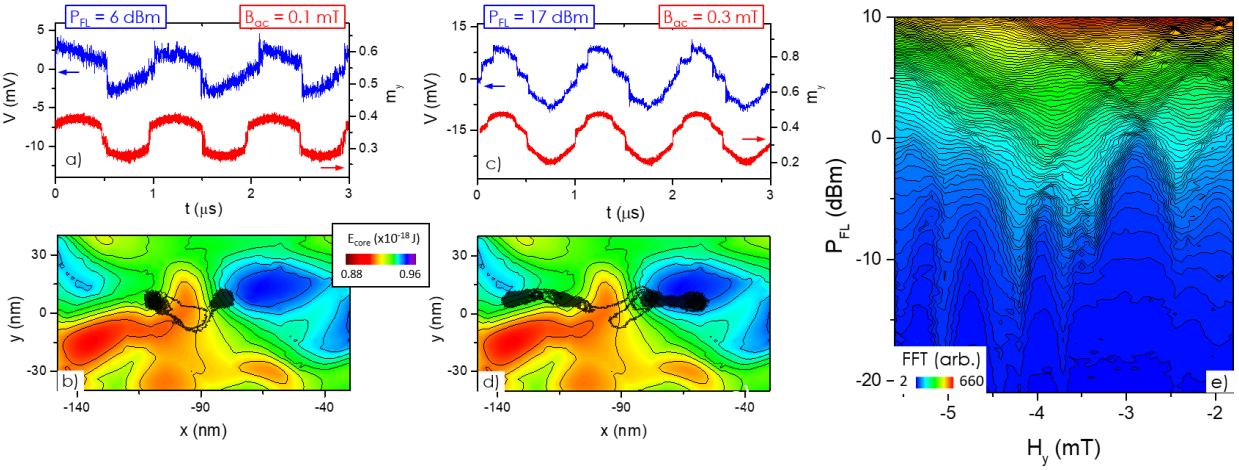

Figure 9 – experimental voltage and simulated magnetisation component along the y-axis as a function of time showing the system respond to the 1 MHz locking signal for a) PFL = 6 dBm and Bac = 0.1 mT and c) PFL = 17 dBm and Bac = 0.3 mT as well as the simulated vortex core trajectory transposed on the energy landscape for b) Bac = 0.1 mT and d) Bac = 0.3 mT. e) The FFT magnitude at 1MHz is plotted as a function of the locking power and in-plane magnetic field.

The demonstration that the vortex core can be locked to an external driving signal is explored in more detail in Figure 10, where, unlike Figure 9, the locking 1 MHz signal is now applied directly to the MTJ, rather than the vertically integrated field line. A similar locking effect is observed, this time where the locking mechanism is due to the Oested and spin-torque terms [14,23]. In Figure 10 a) the resistance measured with a dc current of 0.1 mA is plotted as a function of the in-plane field, and the jumps which correspond to the fields at which the vortex core is in the super-paramagnetic regime are visible, as discussed previously in Figure 8. In Figure 10 b), no dc bias is applied, but instead an AC signal (f = 1 MHz, P_{FL} = -20 dBm) is applied, and peaks in the rectified voltage are visible. When the driving AC current causes the vortex core to become locked and switch between different pinning

This project has received funding from the EU Research and Innovation Programme Horizon Europe under grant agreement No 101070290.

sites, the resultant AC resistance will have a similar frequency to that of the driving current (in this case 1 MHz). The peaks in voltage can, therefore, be understood as being a non-resonant mixing effect, similar to the more commonly reported resonant spin-diode effect [24]. The voltage peaks are only observed at in-plane fields where the resistance changes sharply, i.e. the vortex is behaving super-paramagnetically.

It should be noted that the movement of the vortex core across different pinning sites is an inherently stochastic process, and from one cycle to another the core may pin differently. However, the rectified voltage is time-averaged and shows a very good level of reproducibility, meaning that although there is a stochastic element to the pinning, the nature of the probabilistic effect is such that with sufficient time averaging reproducible data is achievable (the dc voltage measured in this paper was taken over a time window of 20 ms, and as such is an average of 20,000 cycles of the rf current) and shows very good reproducibility.

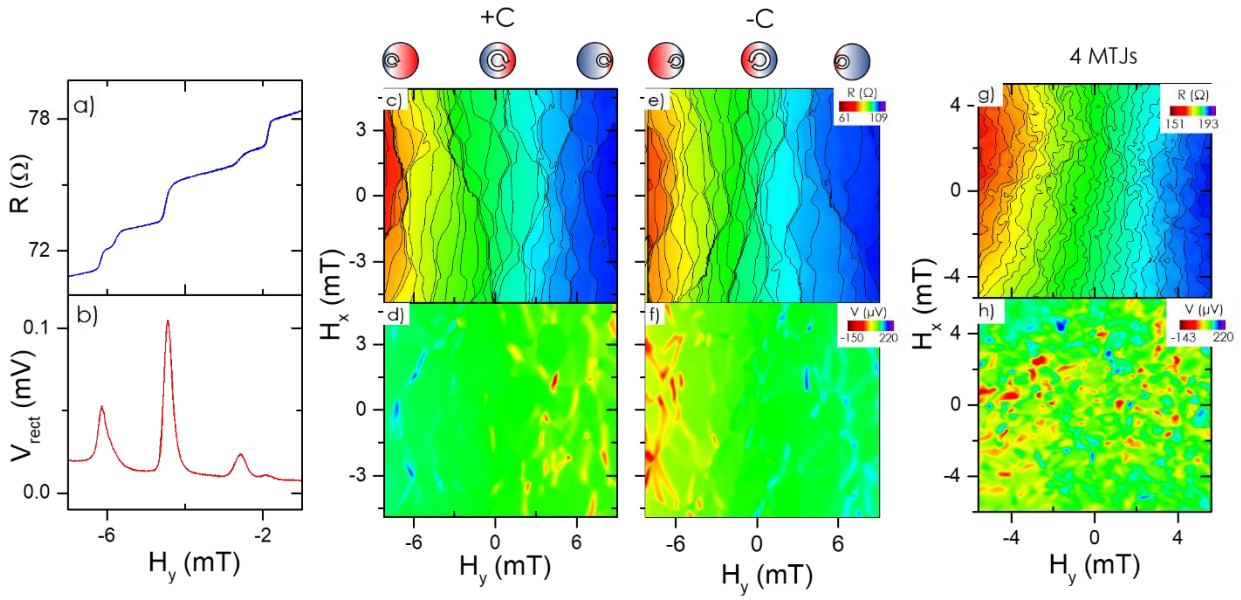

Figure 10 – a) resistance measured with dc current of 0.1 mA and the rectified voltage measured in the absence of a dc bias but with an ac signal of f = 1 MHz, PFL = -20 dBm as a function of an in-plane magnetic field applied along the y-axis. c), e) Resistance and d), f) rectified voltage as a function of in-plane magnetic field applied in both the x and y-axis (i.e. Hx and Hy) for two different vortex chirailities (+C and -C), respectively, in a single MTJ and in-plane magnetic field dependence of the g) resistance and h) the rectified voltage for 4 MTJs.

Having so far only showed the response of the magnetic vortex to a one-dimensional in-plane magnetic field (i.e. aligned collinear with the pinning axis of the MTJ, or y-axis), in Figure 10 we demonstrate the two-dimensional nature of this effect by applying an in-plane magnetic fields along both the x and y-axis. In Figure 10 c) the resistance as a function of the in-plane magnetic field is presented. As the y-axis is aligned collinear to the pinning axis, the resistance is larger for positive fields than negative fields, as shown in Figure 10 a), as more of the vortex aligns with the magnetic field and the vortex core shifts along the x-axis. When the field is applied along the x-axis the magnetisation component of the vortex aligned along the x-axis increases, but this does not result in a change in the device resistance as the fixed layer is only sensitive to variations in the magnetisation

This project has received funding from the EU Research and Innovation Programme Horizon Europe under grant agreement No 101070290.

along the y-axis. The magnetic fields which are applied have been chosen such that the free layer is always in the magnetic vortex state and is not saturated by the field applied in either x or y.

The resistance versus in-plane magnetic field dependence (Figure 10 c) and e)) is presented for both the vortex chiralities (i.e. sense of in-plane rotation, clockwise or counter-clockwise) and show many different separate regions with a relatively small resistance versus field dependence, corresponding to the vortex core being strongly pinned. These plateaus are separated by boundaries of large resistance variation, corresponding to the super-paramagnetic transition region. Resistively the different chiralities are mostly equivalent, but in reality although a positive in-plane magnetic field applied along the y-axis will increase the magnetisation component aligned along the positive y-axis, the vortex core will actually shift in opposite directions for each chirality, meaning that the physical location, and therefore the local energy landscape will be different for each chirality.

This chirality dependence is more pronounced for the rectified voltage for an driving current of 1 MHz and P_{FL} = -20dBm, Figure 10 d) and f) for chirality +C and –C respectively. Similar to Figure 10 b), the voltage shows sharp peaks in the voltage at the regions corresponding to the fields where the resistance varies strongly, i.e. where the core is behaving super-paramagnetically. For negative in-plane magnetic fields the sign of the rectified voltage is negative (i.e. blue) and positive (i.e. red) for positive in-plane magnetic fields for the positive +C chirality. This behaviour is reveresed for the negative chirality (i.e. positive voltage response for a negative in-plane magnetic field). The change in sign can be understood in terms of the phase of the locking, which is different for different chiralities. This sign change, in addition to the absence of peaks at zero in-plane magnetic field (i.e. the vortex core is close to the centre of the pillar), are characteristic signs that the dominant excitation mechnism is the radial Oested field, which has been shown to have a sign change depending on the core offset due to reasons of symmetry, discussed previously in refs. [14,23], as each chirality has a sense of rotation, here defined as being positive, i.e. +C, if it is along the same rotational sense as a positive current flowing vertically in the nanopillar.

3.1.5 Physically unclonable functions

Physically unclonable functions (PUFs) [25,26] are an emerging concept which utilise specific impossible to replicate physical hardware properties in a system to generate a unique response when challenged. There are many examples of such systems in the literature, including SRAM [27], Phase Change Memory (PCM-RAM) [28] and Spin Transfer Torque (STT-RAM) [29]. Whilst the proposed PUFs come from a wide range of scientific disciplines, the common element between them is that when a specific challenge is made to the system, a paired response will be generated which is unique to the particular system, exploiting inherent random variations which are introduced during fabrication. This Challenge-Response Pair (CRP) acts as a fingerprint which is an essential part of the authentication process required for secure communication. So far, all these systems explore variations that can be measured in large ensembles of individual devices as in the case of the initial power up configuration of single bits in large memory arrays.

In this report, a magnetic vortex based physically unclonable function (vPUF) is proposed, where the complex energy landscape generated by the interaction between the magnetic vortex and the

granular defects results in complex non-linear dynamics which can then be used to create an extremely high dimensional CRP parameter space within a single nanodevice, shown schematically in Figure 11.

By applying a current to a vertically integrated field line above the MTJ, an in-plane magnetic field will occur at the vortex-based magnetic tunnel junction located below. The magnetic vortex is composed of in-plane components oriented 360º, and the in-plane magnetic field will act to displace the central magnetic vortex core as the in-plane part of the vortex aligns with the magnetic field. Due the presence of granular defects, there exists a complex energy landscape due to variations in the magnetisation and exchange stiffness between grains [9]. The vortex core interacts strongly with these local complex energy landscape and can produce a strongly non-linear response which will be the unique output of the vPUF.

In fact the impact of the granular defects are so pronounced that there are several different physical properties which could be used as the response of a vPUF, namely;

1) The resonant frequency of the MTJ has been shown to vary strongly with the granular defects [9] and whilst this can be easily measured in a lab environment with a spectrum analyser or via the spin-diode effect, measuring the device frequency can be difficult for integration with electronics.

2) The MTJ resistance also varies with the granular defects and is relatively easy to measure, however, the variation in resistance of the MTJ due to the grains is not particularly strong and problems will occur due to different devices not demonstrating sufficient variability.

3) A rectified voltage can be generated when the vortex core is loosely pinned regime and locks to an external signal. This voltage is relatively easy to measure and can be strongly non-linear.

This project has received funding from the EU Research and Innovation Programme Horizon Europe under grant agreement No 101070290.

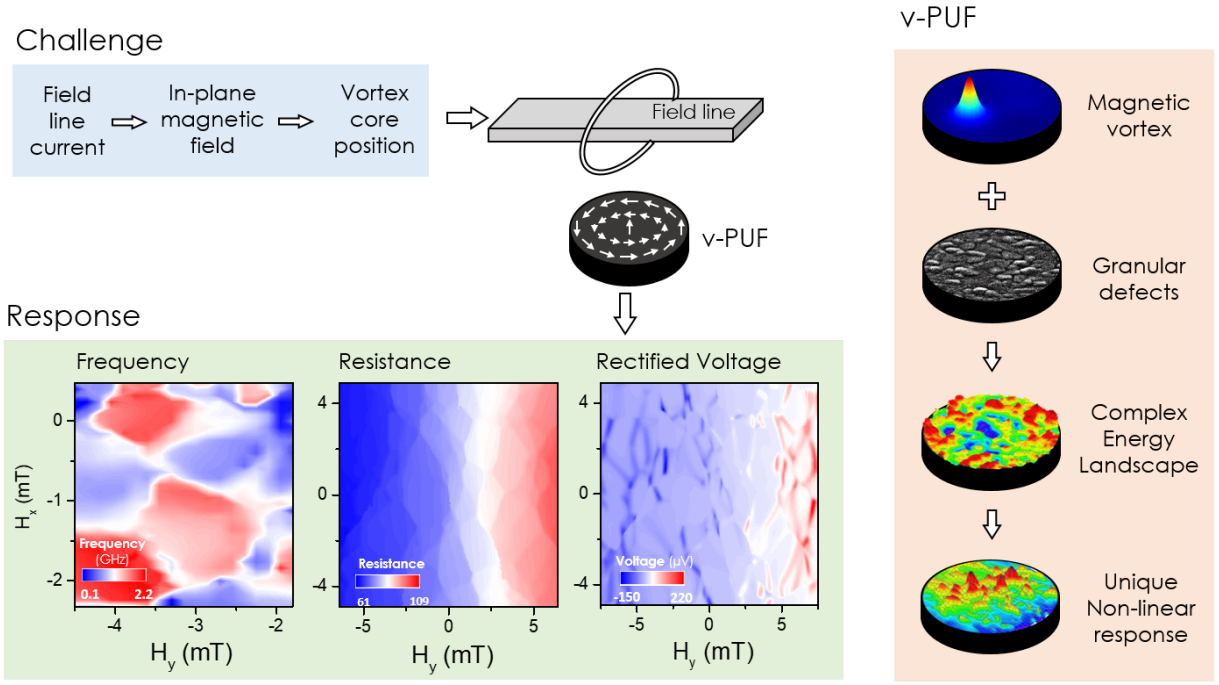

Figure 11 – schematic representation of the vPUF concept, where an input challenge (i.e. current applied to an integrated field line) results in a displacement of the vortex core, which then produces a unique non-linear output response

One of the key advantages of the vPUF compared to other spintronics-based PUFs is that the vPUF magnetic tunnel junction stack has already been used to demonstrate a high frequency oscillator [17], detector [18], random number generator [19] and sensor [20]. This multi-functional stack allows individual devices to perform different functionalities depending the input, or for multiple devices using the same stack to be easily integrated with CMOS via a single growth deposition. Of particular importance is the fact that Vortex MTJs identical to those explored in this paper have been used to implement RF communication schemes [18,21], meaning that these devices have a high potential to implement secure communications where the vortex devices taking part in the DC->RF or RF->DC transducer components can be uniquely and unambiguously identified.

3.1.6 Amelioration of the granular defects using amorphous ferromagnets

Having identified the challenge posed by local pinning sites in vortex-based magnetic tunnel junctions, we now present two potential solutions for reducing the impact of these local energy minima on the vortex dynamics; removing granular defects by using an amorphous free layer and reducing the impact of the interface by increasing the free layer thickness. The work presented in the first half of this report uses a CoFeB/Ta/NiFe composite free layer, where the polycrystalline NiFe is chosen due to its magnetic softness, and the CoFeB is selected to ensure good texture in the insulating MgO barrier, and therefore subsequent high tunneling magnetoresistance. The CoFeB is amorphous as deposited, but crystalises into bcc (001) during the annealing which is an essential step

This project has received funding from the EU Research and Innovation Programme Horizon Europe under grant agreement No 101070290.

to ensure high TMRs above 100%. The Ta layer is to ensure a separation of crystalinity between the NiFe and the CoFeB.

Whilst the CoFeB/Ta/NiFe composite layer has shown good results for large power excitations, the polycrstaline nature of the free layer results in additional pinning sites. In order to avoid this, an amorphous soft magnetic layer has been selected to replace the NiFe, namely CoFeSiB. $Co_{67}Fe_4Si_{14.5}B_{14.5}$ is an interesting candidate for magnetic tunnel junctions as it is amorphous after standard annealing processes [31] and has been previously investigated in micron-sized AlO-based magnetic tunnel junctions where lower switching fields were observed [32–34]. Figure 12 a) and b) shows the x-ray diffraction measurement of two thin films, NiFe and CoFeSiB respectively, after annealing at 330°C. A clear peak associated with fcc (111) is observed for the polycrystalline NiFe, whereas no peak is observed for the CoFeSiB.

As well as being amorphous in unpatterned thin films, in Figure 12 c) and d) the cross sectional transmission electron microscopy (TEM) is presented for two patterned magnetic tunnel junction devices, with c) CoFeB/Ta/NiFe and d) CoFeB/Ta/CoFeSiB free layers. By analysis of the Fast Fourier Transform (FFT), the NiFe image is shown to be consistent with an orthorhombic crystal with 111 zone axis, whilst the CoFeSiB appears amorphous after patterning and annealing.

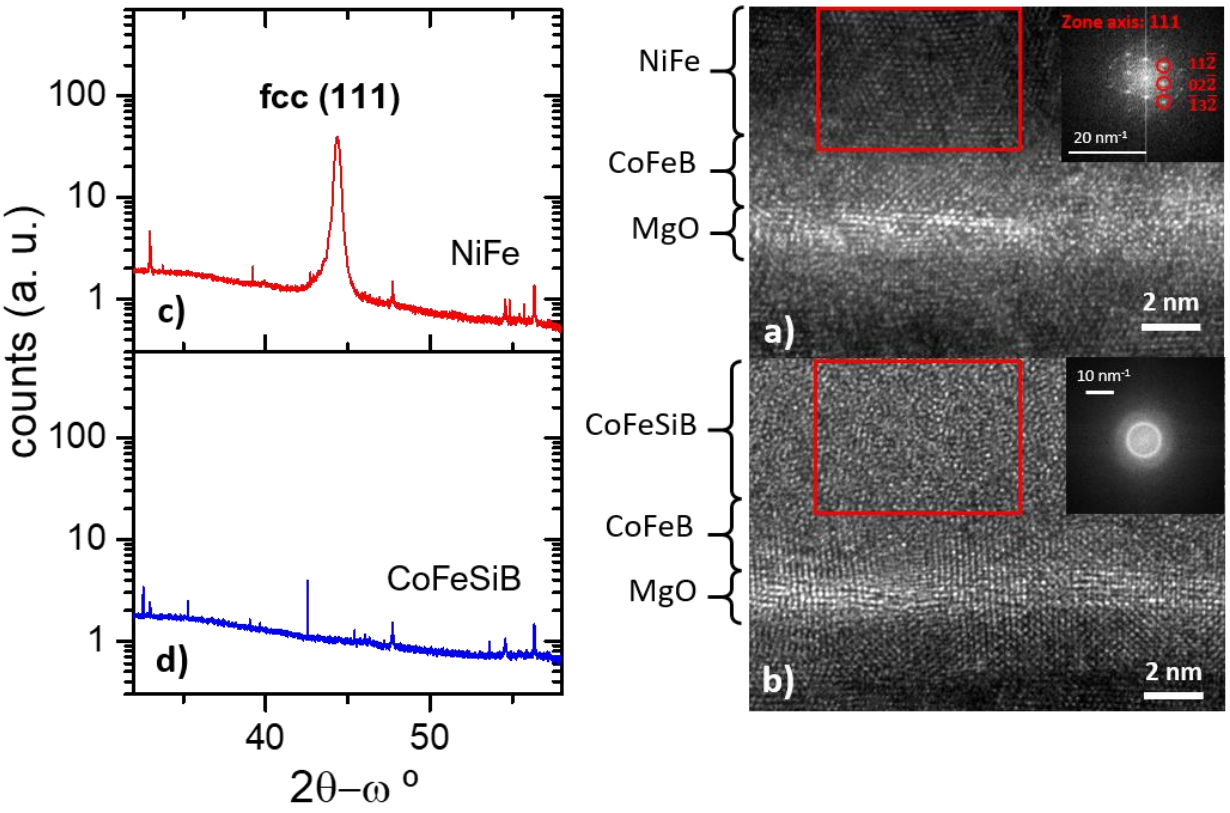

Figure 12 – NiFe and CoFeSiB crystallography comparison - x-ray diffraction pattern of a) NiFe and b) CoFeSiB annealed thin films as well as cross sectional TEM images of two patterned magnetic tunnel junction devices with c) CoFeB/Ta/NiFe and d) CoFeB/Ta/CoFeSiB free layers.

This project has received funding from the EU Research and Innovation Programme Horizon Europe under grant agreement No 101070290.

Having identified CoFeSiB as an amorphous free layer, even after annealing, nano-devices were patterned and their resonant frequency was investigated via the spin diode effect (with an rf current of P_{rf} = 1 µW). As seen in Figure 13 a), the CoFeB(2.0)/Ta(0.5)/NiFe(7.0 nm) shows the sub-threshold behaviour, with a drastic variation of the resonant frequency as a function of the in-plane magnetic field, as the core moves from one pinning site to another, each with markedly different energy landscapes and therefore resonant frequencies. When the NiFe is replaced with CoFeSiB(18 nm), shown in Figure 13 b), the resonant frequency is seen to still vary significantly as a function of the in-plane magnetic field but with the impact being reduced by the amorphous nature of the CoFeSiB. Whilst there still exists a variation in frequency, this can be seen to be between 0.1 - 1 GHz (relative to the 0.1 – 2.5 GHz of the NiFe). The fact that the vortex continues to be in the sub-threshold pinned regime even with an amorphous free layer suggests that the impact of interfacial roughness and the polycrystalline CoFeB are still playing an important role in the energy landscape. In Figure 13 c), the thickness of the CoFeSiB is increased to 80 nm and the variation in resonant frequency can be seen to drastically reduce, with the spin diode response being observed mostly between 0.5 – 0.6 GHz, demonstrating a substantial reduction of frequency variation due to the local pinning sites.

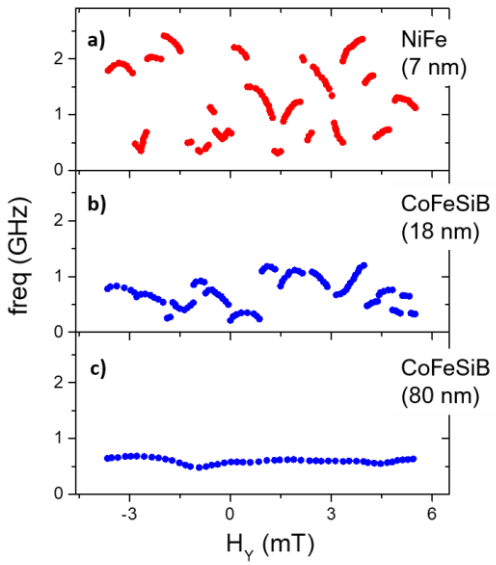

Figure 13 – Frequency variation reduction in amorphous free layers - The measured resonant frequency as a function of the in-plane magnetic field for the magnetic tunnel junctions of 400 nm diameter, with a free layer comprised of a) CoFeB(2.0)/Ta(0.5)/NiFe(7 nm), b) CoFeB(2.0)/Ta(0.5)/CoFeSiB(18 nm) and c) CoFeB(2.0)/Ta(0.5)/CoFeSiB(80 nm)

The reduction of the frequency variation as a function of in-plane magnetic field for the amorphous CoFeSiB free layer is important in the context of rf-based artificial synapses, but the significance goes beyond this particular case, and has more wide ranging implications. The frequency variation can be considered as a measurement of the pinning sites and, therefore, the thick amorphous CoFeSiB shows reduced pinning in general, making it an interesting candidate for further study for a range of technological implementations, for example racetrack memory or magnetic field sensors. Further study is needed to accurately extract the material parameters of CoFeSiB (e.g. damping and

This project has received funding from the EU Research and Innovation Programme Horizon Europe under grant agreement No 101070290.

exchange constant), and one potential drawback with using such thick free layer materials is that the critical current for steady state oscillations will depend on the thickness of the material [28], so that observing the dc to rf transduction may not be possible with such thick layers.

To further explore the reduction in pinning for thicker CoFeSiB, in Figure 14 the absolute value of the rectified spin diode voltage measured at zero applied magnetic field is presented as a function of the rf power and frequency, for four different CoFeSiB thicknesses. The free layer consists of CoFeB(2.0)/Ta(0.5)/CoFeSiB(X nm), where X = 6, 18, 40 and 80 nm for a, b, c and d, respectively. For the thinnest CoFeSiB, the pinning threshold is around P_{rf} = 100 µW, similar to that observed in NiFe (although this threshold varies strongly as a function of the local pinning sites). This threshold reduces to around 20 µW and 4 µW for X = 18 and 40 nm respectively. For the case of X = 80 nm, there is no clear threshold visible and the gyrotropic mode is accessible even down to P_{rf} = 100 nW, which is therefore a gain of around three order of magnitude over the relatively thinner X = 6nm.

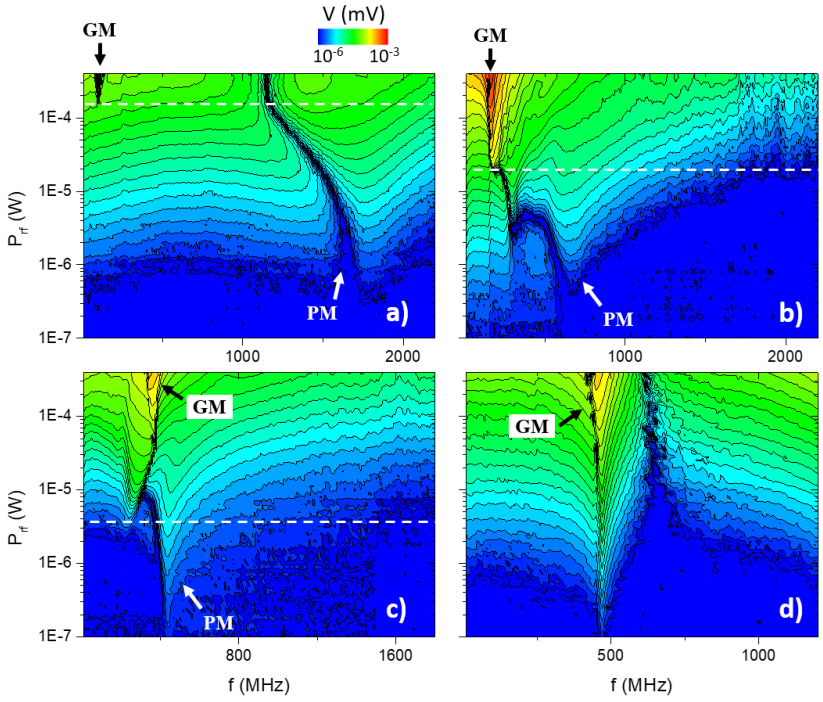

Figure 14 – Pinning threshold reduction with CoFeSiB thickness - a) Absolute magnitude of the experimentally determined spin-diode voltage as a function of the excitation frequency and power with the white line showing the threshold power, P_{rf}^{t}, at which the vortex core escape the pinning site for a free layer of CoFeB(2.0)/Ta(0.5)/CoFeSiB(X nm), where X = a) 6nm, b) 18nm, c) 40nm and d) 80nm. GM signifies the gyrotropic mode and PM represents the pinned mode.

In conclusion, the threshold power required to escape the local pinning sites can be seen in Table 2, where the depinning is seen to be substantially reduced (by up to 3 orders of magnitude) by the use of amorphous CoFeSiB.

This project has received funding from the EU Research and Innovation Programme Horizon Europe under grant agreement No 101070290.

Internal reference	Free layer	Depinning power (µW)
VPW42	CoFeSiB 6nm	100
VPW32	CoFeSiB 18nm	20
VPW46	CoFeSiB 40nm	4
VPW32	CoFeSiB 80nm	0.1
VPW43	NiFe 7nm	60

Table 2 – comparison of the de-pinning rf power for different materials and thicknesses

4 Conclusion and future perspectives

Vortex-based magnetic tunnel junctions are particularly sensitive to granular defects owing to the small size of the vortex core and its sensitivity to relatively small changes in local material conditions such as saturation magnetisation and exchange coupling. This sensitivity results in pronounced behaviour which would deviate from a standard analytical model of the magnetic vortex. Micromagnetic simulations can well model this behaviour which a strong impact on both the static resistance and dynamic properties of the device. Whilst there is potential for the grains to add high dimensionality to the reservoirs, the pinning and depinning at the local defect induced energy minima can be strongly stochastic, which is detrimental to time series analysis. Moving to thicker CoFeSiB is an interesting strategy for defect mitigation, and additionally the devices are being explored in a new direction in the context of cryptography and physical unclonable functions.

5 Bibliography

[1] A. S. Jenkins, L. S. E. Alvarez, P. P. Freitas, and R. Ferreira, Nanoscale true random bit generator based on magnetic state transitions in magnetic tunnel junctions, Sci. Rep. **9**, 15661 (2019).

[2] A. Litvinenko, V. Iurchuk, P. Sethi, S. Louis, V. Tyberkevych, J. Li, A. Jenkins, R. Ferreira, B. Dieny, A. Slavin, and U. Ebels, Ultrafast Sweep-Tuned Spectrum Analyzer with Temporal Resolution Based on a Spin-Torque Nano-Oscillator, Nano Lett. **20**, 6104 (2020).

[3] A. S. Jenkins, L. San Emeterio Alvarez, R. Dutra, R. L. Sommer, P. P. Freitas, and R. Ferreira, Wideband High-Resolution Frequency-to-Resistance Converter Based on Nonhomogeneous Magnetic-State Transitions, Phys. Rev. Appl. **13**, 014046 (2020).

[4] a. S. Jenkins, R. Lebrun, E. Grimaldi, S. Tsunegi, P. Bortolotti, H. Kubota, K. Yakushiji, a. Fukushima, G. de Loubens, O. Klein, S. Yuasa, and V. Cros, Spin torque resonant vortex core expulsion for an efficient radio-frequency detection scheme, Nat. Nanotechnol. 1 (2015).

[5] L. Martins, A. S. Jenkins, J. Borme, J. Ventura, P. P. Freitas, and R. Ferreira, Second harmonic injection locking of coupled spin torque vortex oscillators with an individual phase access, Commun. Phys. 2023 61 **6**, 1 (2023).

This project has received funding from the EU Research and Innovation Programme Horizon Europe under grant agreement No 101070290.

[6] A. S. Jenkins, L. S. E. Alvarez, S. Memshawy, P. Bortolotti, V. Cros, P. P. Freitas, and R. Ferreira, Electrical characterisation of higher order spin wave modes in vortex-based magnetic tunnel junctions, Commun. Phys. 2021 41 **4**, 1 (2021).

[7] M. Stebliy, A. Jenkins, L. Benetti, E. Paz, and R. Ferreira, Non-Volatile Analog Control and Reconfiguration of a Vortex Nano-Oscillator Frequency, Adv. Funct. Mater. **34**, 2405776 (2024).

[8] A. S. Jenkins, L. Martins, L. Benetti, A. Schulman, P. Anacleto, M. Claro, E. Paz, I. Çaha, F. L. Deepak, and R. Ferreira, The impact of local pinning sites in magnetic tunnel junctions with non-homogeneous free layers, (2023).

[9] A. S. Jenkins, L. Martins, L. C. Benetti, A. Schulman, P. Anacleto, M. S. Claro, I. Caha, F. L. Deepak, E. Paz, and R. Ferreira, The impact of local pinning sites in magnetic tunnel junctions with non-homogeneous free layers, Commun. Mater. 2024 51 **5**, 1 (2024).

[10] T. Y. Chen, M. J. Erickson, P. A. Crowell, and C. Leighton, Surface roughness dominated pinning mechanism of magnetic vortices in soft ferromagnetic films, Phys. Rev. Lett. **109**, 097202 (2012).

[11] M. Möller, J. H. Gaida, and C. Ropers, Pinning and gyration dynamics of magnetic vortices revealed by correlative Lorentz and bright-field imaging, Phys. Rev. Res. **4**, 013027 (2022).

[12] R. L. Compton and P. A. Crowell, Dynamics of a pinned magnetic vortex, Phys. Rev. Lett. **97**, 137202 (2006).

[13] J. S. Kim, O. Boulle, S. Verstoep, L. Heyne, J. Rhensius, M. Kläui, L. J. Heyderman, F. Kronast, R. Mattheis, C. Ulysse, and G. Faini, Current-induced vortex dynamics and pinning potentials probed by homodyne detection, Phys. Rev. B - Condens. Matter Mater. Phys. **82**, 104427 (2010).

[14] L. Martins, A. S. Jenkins, L. S. E. Alvarez, J. Borme, T. Böhnert, J. Ventura, P. P. Freitas, and R. Ferreira, Non-volatile artificial synapse based on a vortex nano-oscillator, Sci. Reports 2021 111 **11**, 1 (2021).

[15] T. Y. Chen, A. T. Galkiewicz, and P. A. Crowell, Phase diagram of magnetic vortex dynamics, Phys. Rev. B **85**, 180406 (2012).

[16] S. Tsunegi, K. Yakushiji, A. Fukushima, S. Yuasa, and H. Kubota, Microwave emission power exceeding 10 μ W in spin torque vortex oscillator, Appl. Phys. Lett. **109**, 252402 (2016).

[17] D. Marković, N. Leroux, A. Mizrahi, J. Trastoy, V. Cros, P. Bortolotti, L. Martins, A. Jenkins, R. Ferreira, and J. Grollier, Detection of the Microwave Emission from a Spin-Torque Oscillator by a Spin Diode, Phys. Rev. Appl. **13**, 044050 (2020).

[18] A. Dussaux, A. V Khvalkovskiy, P. Bortolotti, J. Grollier, V. Cros, and A. Fert, Field dependence of spin-transfer-induced vortex dynamics in the nonlinear regime IN THE LINEAR REGIME, **014402**, 1 (2012).

[19] R. P. Cowburn, Superparamagnetism and the future of magnetic random access memory, J. Appl. Phys. **93**, 9310 (2003).

[20] A. Fukushima, T. Seki, K. Yakushiji, H. Kubota, H. Imamura, S. Yuasa, and K. Ando, Spin dice: A scalable truly random number generator based on spintronics, Appl. Phys. Express **7**, 083001

This project has received funding from the EU Research and Innovation Programme Horizon Europe under grant agreement No 101070290.

(2014).

[21] C. Safranski, J. Kaiser, P. Trouilloud, P. Hashemi, G. Hu, and J. Z. Sun, Demonstration of Nanosecond Operation in Stochastic Magnetic Tunnel Junctions, Nano Lett. **17**, 11 (2021).

[22] A. Mizrahi, N. Locatelli, R. Lebrun, V. Cros, A. Fukushima, H. Kubota, S. Yuasa, D. Querlioz, and J. Grollier, Controlling the phase locking of stochastic magnetic bits for ultra-low power computation, Sci. Reports 2016 61 **6**, 1 (2016).

[23] A. S. Jenkins, L. S. E. Alvarez, S. Memshawy, P. Bortolotti, V. Cros, P. P. Freitas, and R. Ferreira, Electrical characterisation of higher order spin wave modes in vortex-based magnetic tunnel junctions, Commun. Phys. 2021 41 **4**, 1 (2021).

[24] A. A. Tulapurkar, Y. Suzuki, A. Fukushima, H. Kubota, H. Maehara, K. Tsunekawa, D. D. Djayaprawira, N. Watanabe, and S. Yuasa, Spin-torque diode effect in magnetic tunnel junctions, Nature **438**, 339 (2005).

[25] T. McGrath, I. E. Bagci, Z. M. Wang, U. Roedig, and R. J. Young, A PUF taxonomy, Appl. Phys. Rev. **6**, 11303 (2019).

[26] Y. Gao, S. F. Al-Sarawi, and D. Abbott, Physical unclonable functions, Nat. Electron. 2020 32 **3**, 81 (2020).

[27] J. Guajardo, S. S. Kumar, G. J. Schrijen, and P. Tuyls, FPGA intrinsic PUFs and their use for IP protection, Lect. Notes Comput. Sci. (Including Subser. Lect. Notes Artif. Intell. Lect. Notes Bioinformatics) **4727 LNCS**, 63 (2007).

[28] L. Zhang, Z. H. Kong, and C. H. Chang, PCKGen: A Phase Change Memory based cryptographic key generator, Proc. - IEEE Int. Symp. Circuits Syst. 1444 (2013).

[29] L. Zhang, X. Fong, C. H. Chang, Z. H. Kong, and K. Roy, Highly reliable memory-based Physical Unclonable Function using Spin-Transfer Torque MRAM, Proc. - IEEE Int. Symp. Circuits Syst. 2169 (2014).

[30] J. A. J. Burgess, A. E. Fraser, F. Fani Sani, D. Vick, B. D. Hauer, J. P. Davis, and M. R. Freeman, Quantitative magneto-mechanical detection and control of the Barkhausen effect, Science (80-.). **339**, 1051 (2013).

[31] J. Ding, G. N. Kakazei, X. Liu, K. Y. Guslienko, and A. O. Adeyeye, Higher order vortex gyrotropic modes in circular ferromagnetic nanodots, 1 (2014).

[32] A. S. Jenkins, E. Grimaldi, P. Bortolotti, R. Lebrun, H. Kubota, K. Yakushiji, A. Fukushima, G. de Loubens, O. Klein, S. Yuasa, and V. Cros, Controlling the chirality and polarity of vortices in magnetic tunnel junctions, Appl. Phys. Lett. **105**, 172403 (2014).

This project has received funding from the EU Research and Innovation Programme Horizon Europe under grant agreement No 101070290.